

A discrete interaction model/quantum mechanical method for simulating surface-enhanced Raman spectroscopy

John L. Payton, Seth M. Morton, Justin E. Moore, and Lasse Jensen

Citation: *The Journal of Chemical Physics* **136**, 214103 (2012); doi: 10.1063/1.4722755

View online: <https://doi.org/10.1063/1.4722755>

View Table of Contents: <http://aip.scitation.org/toc/jcp/136/21>

Published by the [American Institute of Physics](#)

Articles you may be interested in

[A discrete interaction model/quantum mechanical method to describe the interaction of metal nanoparticles and molecular absorption](#)

The Journal of Chemical Physics **135**, 134103 (2011); 10.1063/1.3643381

[A discrete interaction model/quantum mechanical method for describing response properties of molecules adsorbed on metal nanoparticles](#)

The Journal of Chemical Physics **133**, 074103 (2010); 10.1063/1.3457365

[Theory and method for calculating resonance Raman scattering from resonance polarizability derivatives](#)

The Journal of Chemical Physics **123**, 174110 (2005); 10.1063/1.2046670

[A discrete solvent reaction field model within density functional theory](#)

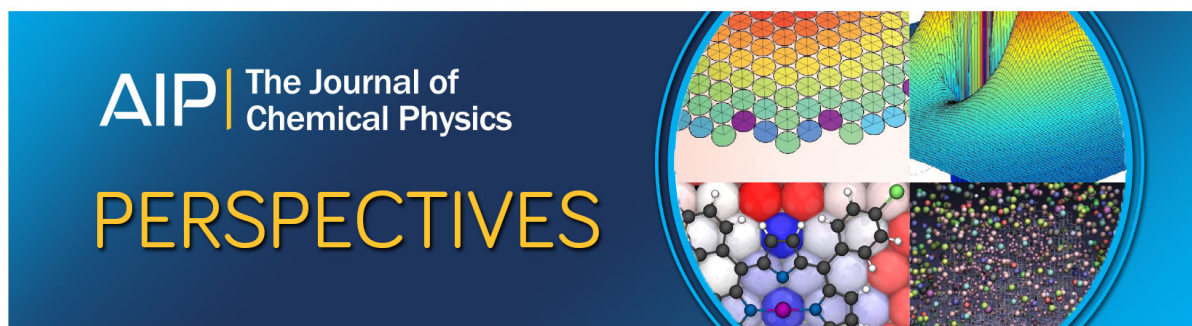
The Journal of Chemical Physics **118**, 514 (2003); 10.1063/1.1527010

[Simulation of resonance hyper-Rayleigh scattering of molecules and metal clusters using a time-dependent density functional theory approach](#)

The Journal of Chemical Physics **141**, 124305 (2014); 10.1063/1.4895971

[A discrete solvent reaction field model for calculating molecular linear response properties in solution](#)

The Journal of Chemical Physics **119**, 3800 (2003); 10.1063/1.1590643



A discrete interaction model/quantum mechanical method for simulating surface-enhanced Raman spectroscopy

John L. Payton, Seth M. Morton, Justin E. Moore, and Lasse Jensen^{a)}

Department of Chemistry, The Pennsylvania State University, 104 Chemistry Building, University Park, Pennsylvania 16802-4615, USA

(Received 25 March 2012; accepted 14 May 2012; published online 4 June 2012)

We have derived and implemented analytical gradients for the discrete interaction model/quantum mechanics (DIM/QM) method. DIM/QM combines an atomistic electrodynamics model with time-dependent density functional theory and thus enables modeling of the optical properties for a molecule while taking into account the local environment of a nanoparticle's surface. The DIM/QM analytical gradients allow for geometry optimizations, vibrational frequencies, and Raman spectra to be simulated for molecules interacting with metal nanoparticles. We have simulated the surface-enhanced Raman scattering (SERS) spectra for pyridine adsorbed on different sites of icosahedral nanoparticles with diameters between 1 and 8 nm. To describe the adsorption of the pyridine molecule onto the metal surface, we have implemented a coordination-dependent force field to differentiate the various local surface environments. We find that the DIM/QM method predicts geometries and frequencies that are in good agreement with full QM simulations and experiments. For the simulated SERS spectra of pyridine, we find a significant dependence on the adsorption site and the size of the metal nanoparticle. This illustrates the importance of accounting for the local environment around the molecule. The Raman enhancement factors are shown to roughly mirror the magnitude of the nanoparticle's local field about the molecule. Because the simulated nanoparticles are small, the plasmon peaks are quite broad which results in weak local electric fields and thus modest Raman enhancement factors. © 2012 American Institute of Physics. [<http://dx.doi.org/10.1063/1.4722755>]

I. INTRODUCTION

Noble metal nanoparticles have a broad range of applications in optics, molecular sensors, catalysis, and therapeutic agents due to their ability to amplify the electromagnetic fields near the metal surface through the excitation of a localized surface plasmon resonance, known as the optical antenna effect.^{1–13} Because of the tunability of a plasmon with nanoparticle's shape, size, and/or environment, optical antennas may be used to interact with a wide variety of molecules.¹⁴ The enhanced local field at the surface of the metal nanoparticle can significantly alter the optical properties of molecules located near the surface, especially if there is spectral overlap between the two systems. It is this effect that is exploited in surface-enhanced vibrational spectroscopic techniques such as surface-enhanced Raman scattering (SERS),^{3,11,15,16} in which the Raman scattering of adsorbed molecules can be enhanced by more than $\times 10^{10}$, allowing for single molecule detection.^{17–21} While SERS has been known for over 35 years,^{22,23} the intricate details of the enhancement mechanisms are still being debated due to the complicated nature of the metal-molecule interface.^{24,25}

The SERS enhancement is the result of two types of enhancement mechanisms. The first is the electromagnetic mechanism (EM), in which a strong local field due to the plasmon excitation enhances the Raman scattering.^{24,25} It can be shown that the Raman scattering scales as $|E|^4$ when only the EM is considered.^{24,26,27} The second mechanism is the

chemical mechanism (CM), resulting from the overlap between the wavefunctions of the molecule and the metal nanoparticle. The CM can be further classified as resulting from a charge transfer mechanism, a non-resonant chemical mechanism, and/or a molecular resonance mechanism.^{24,25} The CM is difficult to characterize because it depends critically on the exact nature of the local environment in which the molecule binds. Furthermore, the total SERS enhancement is largely dominated by the EM and thus many studies focus only on this mechanism.

Since the EM is considered to only depend on the local field at the surface of the nanoparticle, it is largely independent of the molecule and thus typically studied by simulating the local electric field due to the plasmon excitation using classical electrodynamics.²⁸ Classical electrodynamics provides a good description for the optical properties of these nanoparticles; however, when their dimensions become smaller than 10 nm, quantum size effects become important.^{29–32} In most cases, the nanoparticle and the molecular layer are assumed to be continuous objects characterized by their frequency-dependent dielectric functions with an abrupt interface between the two systems. This completely neglects any microscopic details at the interface, preventing a realistic description of the molecules adsorbing onto the nanoparticles. First-principles simulations enable a detailed understanding of the microscopic environment, but can only be used for small metal clusters.^{24,25,33,34} Thus, a hybrid approach that bridges the microscopic quantum methods and the macroscopic electrodynamics methods is ideally suited for studying SERS.

^{a)}Electronic mail: jensen@chem.psu.edu.

There exists several different hybrid methods that combine a quantum mechanical description of the molecule and a classical description of the metal nanoparticle.^{35–46} These methods offer a realistic treatment of the molecule and the nanoparticle while they take into account the coupling between the two systems. The nanoparticle is often treated as a continuum or on a regular grid; however, using these approximations the specific interactions due to the local environment of the adsorption site cannot be accounted for. To include these interactions, we have been developing the discrete interaction model/quantum mechanics (DIM/QM) method which combines an atomistic electrodynamics model^{47,48} with time-dependent density functional theory (TDDFT).^{49,50} DIM/QM differs from most other hybrid methods by representing the nanoparticle atomistically, allowing us to model the influence of the nanoparticle surface's local environment on the optical properties of a molecule. Previous studies using DIM/QM have explored excitation energies of rhodamine-6G and crystal violet interacting with quasi spherical silver and gold nanoparticles⁴⁹ and enhanced molecular absorption due to the coupling between the molecular and plasmon excitations.⁵⁰

In this work, we derive and implement analytical gradients for DIM/QM, such that geometry optimization, vibrational frequencies, and Raman spectra can be simulated for molecules interacting with metal nanoparticles. As an initial study with this new implementation, we present simulated SERS spectra for pyridine adsorbed on different sites of icosahedral nanoparticles with diameters between 1 and 8 nm. We show that there is a significant dependence on the adsorption site, and it is therefore important to include these local environments when simulating SERS. Furthermore, we show that there are significant differences in the simulated SERS spectra between small and large particles, which is important for comparison with experimental results.

II. THEORY

A. The DIM/QM energy

The DIM/QM method can be seen as an extension of traditional polarizable quantum mechanical/molecular mechanics models^{51–53} for describing optical properties of molecules in solution. In the DIM/QM method, the nanoparticle is considered as a collection of N interacting atoms that when combined describe the total optical response. Each atom is characterized by an atomic polarizability and an atomic capacitance. These intrinsic atomic properties are obtained by fitting against TDDFT results for small silver clusters ($N < 68$) and thus correctly describe the saturation of the polarizability of the nanoparticle as the size increases.⁴⁷ In contrast to most previous work, this enables us to retain the detailed atomistic structure of the nanoparticle.

In the DIM/QM model the total energy is given by

$$U^{\text{TOT}}[\rho] = U^{\text{QM}}[\rho] + U^{\text{DIM/QM}}[\rho], \quad (1)$$

where $U^{\text{QM}}[\rho]$ is the energy of the quantum mechanical (QM) system and $U^{\text{DIM/QM}}[\rho]$ is the interaction energy between the QM system and the DIM system. Both energy contributions to $U^{\text{TOT}}[\rho]$ are here written as functionals dependent on the

ground state density, ρ . The interaction energy is given by

$$U^{\text{DIM/QM}}[\rho] = U^{\text{POL}}[\rho] + U^{\text{VDW}}, \quad (2)$$

where $U^{\text{POL}}[\rho]$ is the polarization energy (the energy required to induced the dipoles and charges in the DIM system) and U^{VDW} accounts for the dispersion and repulsion energy between the DIM and the QM system. U^{VDW} is treated purely classically and thus does not depend on the ground state density. The polarization energy for a nanoparticle with zero total charge ($q^{\text{DIM}} = 0$) is given by classical electrostatics as⁵⁴

$$U^{\text{POL}}[\rho] = -\frac{1}{2} \sum_m^N \mu_{m,\alpha}^{\text{ind}} E_{m,\alpha}^{\text{SCF}} + \frac{1}{2} \sum_m^N q_m^{\text{ind}} V_m^{\text{SCF}}, \quad (3)$$

where μ^{ind} and q^{ind} are the induced dipoles and charges on the DIM atoms respectively, and $E_{m,\alpha}^{\text{SCF}}$ and V_m^{SCF} are the electric field and potential arising from the QM system given by

$$E_{m,\alpha}^{\text{SCF}} = E_{m,\alpha}^{\text{QM,el}} + E_{m,\alpha}^{\text{QM,nuc}}, \quad (4)$$

$$V_m^{\text{SCF}} = V_m^{\text{QM,el}} + V_m^{\text{QM,nuc}}, \quad (5)$$

where $E_{m,\alpha}^{\text{QM,el}}$ and $V_m^{\text{QM,el}}$ arise from the QM electrons

$$E_{m,\alpha}^{\text{QM,el}} = \int \rho(\mathbf{r}_j) \frac{r_{jm,\alpha}}{|\mathbf{r}_{jm}|^3} d\mathbf{r}_j = - \int \rho(\mathbf{r}_j) T_{jm,\alpha}^{(1)} d\mathbf{r}_j, \quad (6)$$

$$V_m^{\text{QM,el}} = \int \frac{\rho(\mathbf{r}_j)}{|\mathbf{r}_{jm}|} d\mathbf{r}_j = \int \rho(\mathbf{r}_j) T_{jm}^{(0)} d\mathbf{r}_j, \quad (7)$$

and $E_{m,\alpha}^{\text{QM,nuc}}$ and $V_m^{\text{QM,nuc}}$ from the QM nuclei

$$E_{m,\alpha}^{\text{QM,nuc}} = \sum_J \frac{Z_J r_{Jm,\alpha}}{|\mathbf{r}_{Jm}|^3} = - \sum_J Z_J T_{Jm,\alpha}^{(1)}, \quad (8)$$

$$V_m^{\text{QM,nuc}} = \sum_J \frac{Z_J}{|\mathbf{r}_{Jm}|} = \sum_J Z_J T_{Jm}^{(0)}, \quad (9)$$

where we introduce the interaction tensors describing the relative distance and orientation between the atoms, given generally as

$$T_{kl,\alpha_1,\dots,\alpha_n}^{(n)} = \nabla_{kl,\alpha_1} \dots \nabla_{kl,\alpha_n} \left(\frac{1}{|\mathbf{r}_{kl}|} \right). \quad (10)$$

We are using the subscripts m and n to denote DIM atoms, I and J to denote QM nuclei, i and j to denote QM electrons, and α, β , etc. to denote arbitrary Cartesian components. \mathbf{r}_k is the vector distance to point k from the origin, and \mathbf{r}_{kl} is the vector distance between points k and l defined as $\mathbf{r}_{kl} = \mathbf{r}_l - \mathbf{r}_k$. $|\mathbf{r}|$ represents a scalar distance defined as $|\mathbf{r}| = \sqrt{r_x^2 + r_y^2 + r_z^2}$.

The induced dipoles and charges needed to calculate the polarization energy are found by solving a set of $4N + 1$ linear equations expressed in super-matrix notation as

$$\begin{pmatrix} \mathbf{A} & -\mathbf{M} & \mathbf{0} \\ -\mathbf{M}^T & -\mathbf{C} & \mathbf{1} \\ \mathbf{0} & \mathbf{1} & \mathbf{0} \end{pmatrix} \begin{pmatrix} \boldsymbol{\mu}^{\text{ind}} \\ \mathbf{q}^{\text{ind}} \\ \lambda \end{pmatrix} = \begin{pmatrix} \mathbf{E}^{\text{SCF}} \\ \mathbf{V}^{\text{SCF}} \\ q^{\text{DIM}} \end{pmatrix}, \quad (11)$$

where the matrix \mathbf{A} describes the dipole-dipole interactions,

$$A_{mn,\alpha\beta} = \begin{cases} \alpha_{m,\alpha\beta}^{-1} & m = n \\ -T_{mn,\alpha\beta}^{(2)} & m \neq n \end{cases}, \quad (12)$$

the matrix \mathbf{M} describes interactions between dipoles and charges,

$$M_{mn,\alpha} = \begin{cases} 0 & m = n \\ T_{mn,\alpha}^{(1)} & m \neq n \end{cases}, \quad (13)$$

and the matrix \mathbf{C} describes charge-charge interactions,

$$C_{mn} = \begin{cases} c_m^{-1} & m = n \\ T_{mn}^{(0)} & m \neq n \end{cases}. \quad (14)$$

These linear equations are found by variational minimization of the classical energy for a collection of interacting atoms described by their atomic polarizability and capacitance under the constraint that the total charge of the system is fixed using the Lagrangian multiplier, λ .⁴⁷

Variational minimization of the total energy given by Eq. (1) leads to the following effective Kohn-Sham operator, $h_{\text{KS}}[\rho(\mathbf{r}_j)]$, given by

$$h_{\text{KS}}[\rho(\mathbf{r}_j)] = -\frac{1}{2}\nabla^2 - \sum_j \frac{Z_j}{|\mathbf{r}_j - \mathbf{R}_j|} + \int \frac{\rho(\mathbf{r}_j)}{|\mathbf{r}_j - \mathbf{r}_i|} d\mathbf{r}_i + \frac{\delta E^{XC}}{\delta \rho(\mathbf{r}_j)} + \hat{V}^{\text{DIM}}(\mathbf{r}_j) \quad (15)$$

with the individual terms being, respectively, the kinetic energy, the nuclear potential, the Coulomb potential, the XC-potential (exchange correlation), and the embedding DIM operator ($\hat{V}^{\text{DIM}}(\mathbf{r}_j)$) describing the molecule-metal interactions. The embedding operator is given by

$$\hat{V}^{\text{DIM}}(\mathbf{r}_j) = \hat{V}^{\text{el}}(\mathbf{r}_j) + \hat{V}^{\text{pol}}(\mathbf{r}_j), \quad (16)$$

where the electrostatic operator ($\hat{V}^{\text{el}}(\mathbf{r}_j)$) is given as

$$\hat{V}^{\text{el}}(\mathbf{r}_j) = \sum_m \frac{q_m^{\text{ind}}}{|\mathbf{r}_{jm}|} = \sum_m q_m^{\text{ind}} T_{jm}^{(0)}, \quad (17)$$

and the polarization operator ($\hat{V}^{\text{pol}}(\mathbf{r}_j)$) is given as

$$\hat{V}^{\text{pol}}(\mathbf{r}_j) = - \sum_m \frac{\mu_{m,\alpha}^{\text{ind}} r_{jm,\alpha}}{|\mathbf{r}_{jm}|^3} = \sum_m \mu_{m,\alpha}^{\text{ind}} T_{jm,\alpha}^{(1)}. \quad (18)$$

The perturbation to the density due to the $\hat{V}^{\text{DIM}}(\mathbf{r}_j)$ operator can be thought of as the image field, i.e., the field arising from the dipoles and charges that are induced in the nanoparticle (DIM system) by the presence of the molecule (QM system).

The classical dispersion and repulsion energies between the DIM and QM systems describing the Van der Waals interactions are modeled using the Lennard-Jones (LJ) 12-6 potential found in the assisted model building with energy refinement (AMBER) force field⁵⁵

$$U^{\text{VDW}} = \sum_{Jm} \varepsilon_{Jm} \left[\left(\frac{r_{e,Jm}}{|\mathbf{r}_{Jm}|} \right)^{12} - 2 \left(\frac{r_{e,Jm}}{|\mathbf{r}_{Jm}|} \right)^6 \right], \quad (19)$$

where ε and r_e are the LJ parameters describing the well depth and equilibrium bond length, respectively, between the J th QM atom the m th DIM atom. The parameters are obtained using the standard combination rules: $r_{e,Jm} = r_{e,J} + r_{e,m}$ and $\varepsilon_{Jm} = \sqrt{\varepsilon_J \varepsilon_m}$.

To account for the different environments of the silver atoms in the nanoparticle (i.e., surface, edge, vertex, and core), we chose to include effective coordination dependent LJ parameters given by⁵⁶

$$r_{e,m} = r_{e,0} + (r_{e,1} - r_{e,0}) \frac{\text{MIN}(CN_m, CN_{\text{max}})}{CN_{\text{max}}}, \quad (20)$$

$$\varepsilon_m = \varepsilon_0 + (\varepsilon_1 - \varepsilon_0) \frac{\text{MIN}(CN_m, CN_{\text{max}})}{CN_{\text{max}}}, \quad (21)$$

where CN_{max} is the maximum coordination numbers for the atom type (for silver $CN_{\text{max}} = 12$) and CN_m is the effective coordination number for DIM atom m . The effective coordination number is calculated from⁵⁶

$$CN_m = \sum_{n \neq m}^N f_c(|\mathbf{r}_{mn}|), \quad (22)$$

where the cutoff function is given by

$$f_c(|\mathbf{r}_{mn}|) = \begin{cases} 1 & \text{if } |\mathbf{r}_{mn}| < |\mathbf{r}_{\text{min}}| \\ \frac{1}{2} \left(1 + \cos \left(\frac{\pi (|\mathbf{r}_{mn}| - |\mathbf{r}_{\text{min}}|)}{|\mathbf{r}_{\text{max}}| - |\mathbf{r}_{\text{min}}|} \right) \right) & \text{if } |\mathbf{r}_{\text{min}}| \leq |\mathbf{r}_{mn}| \leq |\mathbf{r}_{\text{max}}|, \\ 0 & \text{if } |\mathbf{r}_{mn}| > |\mathbf{r}_{\text{max}}| \end{cases} \quad (23)$$

which smoothly connects atoms inside and outside of the coordination sphere. The advantage of using an effective coordination number compared to a standard coordination number (i.e., integer value) is that the effective coordination number can account for defects in the nanoparticle. In this scheme, $r_{e,0}$ and ε_0 describe atoms with low coordination numbers such as surface atoms, and $r_{e,1}$ and ε_1 describe atoms with high coordination numbers such as bulk atoms.

The adsorption of pyridine onto a silver surface can occur through either π interactions, i.e., lying flat on the surface, or through the lone pair of the nitrogen, i.e., standing upright on the surface.⁵⁷⁻⁶¹ It is typically assumed that pyridine binds through the lone pair of the nitrogen due to the observation of a vibrational band around 239 cm^{-1} in SERS experiments.^{22,62,63} Therefore, to account for the chemisorption of the pyridine, we employed the coordination dependent scheme when the nitrogen atom comes within a cutoff

distance of a silver atom. The justification of reusing this scheme is that it gives the nitrogen atom a “knowledge” of the coordination environment of the silver atom involved in the bond with the nitrogen atom.

B. The analytical DIM/QM energy gradients

The total analytical DIM/QM gradients are given by

$$\begin{aligned}\nabla_{\delta} U^{\text{TOT}}[\rho] &= \nabla_{\delta} U^{\text{QM}}[\rho] + \nabla_{\delta} U^{\text{DIM/QM}}[\rho] \\ &= \nabla_{\delta} U^{\text{QM}}[\rho] + \nabla_{\delta} U^{\text{POL}}[\rho] + \nabla_{\delta} U^{\text{VDW}},\end{aligned}\quad (24)$$

where ∇_{δ} refers to differentiation of the energy with respect to the δ direction of atom K . The first term is the gradients of the QM system which is well known from the gas phase. The latter two terms comprise the DIM/QM polarization and Van der Waals gradients, respectively.

To obtain the DIM/QM polarization gradients, $\nabla_{\delta} U^{\text{POL}}[\rho]$, it is convenient to rewrite the polarization energy as (following the poly-tensor notation of Applequist⁶⁴)

$$U^{\text{POL}}[\rho] = -\frac{1}{2} \mathcal{E}^T \mathcal{M}, \quad (25)$$

where the electric multipole moments are given by

$$\mathcal{M} = \begin{pmatrix} \mu^{\text{ind}} \\ \mathbf{q}^{\text{ind}} \\ -\lambda \end{pmatrix} \quad (26)$$

and the electric field and potential are

$$\mathcal{E} = \begin{pmatrix} \mathbf{E}^{\text{SCF}} \\ -\mathbf{V}^{\text{SCF}} \\ q^{\text{DIM}} \end{pmatrix}. \quad (27)$$

Likewise the linear equations (Eq. (11)) needed for solving the induced dipoles and charges can be rewritten as

$$\mathcal{D} \mathcal{M} = \mathcal{E}, \quad (28)$$

where the $4N + 1$ super-matrix is given by

$$\mathcal{D} = \begin{pmatrix} \mathbf{A} & -\mathbf{M} & \mathbf{0} \\ \mathbf{M}^T & \mathbf{C} & \mathbf{1} \\ \mathbf{0} & \mathbf{1} & 0 \end{pmatrix}. \quad (29)$$

Note the sign difference in the second row as compared to Eq. (11). This is because the definition of the polarization energy (Eq. (25)) uses the negative potential. From here, we can follow the strategies employed to derive the analytical gradients of various solvent models.^{65–69}

The DIM/QM polarization energy is a function of the induced dipoles, induced charges, and the QM nuclear coordinates. Therefore, the gradients are given by

$$\begin{aligned}\frac{dU^{\text{POL}}[\rho]}{dR_{K,\delta}} &= \frac{\partial U^{\text{POL}}[\rho]}{\partial R_{K,\delta}} + \frac{\partial U^{\text{POL}}[\rho]}{\partial \mu^{\text{ind}}} \times \frac{\partial \mu^{\text{ind}}}{\partial R_{K,\delta}} \\ &\quad + \frac{\partial U^{\text{POL}}[\rho]}{\partial \mathbf{q}^{\text{ind}}} \times \frac{\partial \mathbf{q}^{\text{ind}}}{\partial R_{K,\delta}}.\end{aligned}\quad (30)$$

Fortunately, the polarization energy has been variationally minimized with respect to the changes in the induced dipoles

and charge (i.e., $\frac{\partial U^{\text{POL}}[\rho]}{\partial \mu^{\text{ind}}} = \frac{\partial U^{\text{POL}}[\rho]}{\partial q^{\text{ind}}} = 0$). Thus, only the explicit coordinate dependence needs to be considered for evaluating the gradients.

Differentiation of the DIM/QM polarization energy gives

$$\nabla_{\delta} U^{\text{POL}}[\rho] = \nabla_{\delta} \left(-\frac{1}{2} \mathcal{E}^T \mathcal{M} \right) = -\frac{1}{2} (\nabla_{\delta} \mathcal{E}^T) \mathcal{M} - \frac{1}{2} \mathcal{E}^T (\nabla_{\delta} \mathcal{M}). \quad (31)$$

Next, the induced multipole moments can be written as $\mathcal{M} = \mathcal{D}^{-1} \mathcal{E}$ and substituted into Eq. (31) to give

$$\begin{aligned}\nabla_{\delta} U^{\text{POL}}[\rho] &= -\frac{1}{2} (\nabla_{\delta} \mathcal{E}^T) \mathcal{M} - \frac{1}{2} \mathcal{E}^T (\nabla_{\delta} (\mathcal{D}^{-1} \mathcal{E})) \\ &= -\frac{1}{2} (\nabla_{\delta} \mathcal{E}^T) \mathcal{M} - \frac{1}{2} \mathcal{E}^T (\nabla_{\delta} \mathcal{D}^{-1}) \mathcal{E} \\ &\quad - \frac{1}{2} \mathcal{E}^T \mathcal{D}^{-1} (\nabla_{\delta} \mathcal{E}).\end{aligned}\quad (32)$$

The classical interaction matrix here is independent of the QM coordinates, and thus we have $\nabla_{\delta} \mathcal{D} = 0$ (or $\nabla_{\delta} \mathcal{D}^{-1} = 0$). The DIM/QM polarization gradients then reduce to

$$\nabla_{\delta} U^{\text{POL}}[\rho] = -(\nabla_{\delta} \mathcal{E}^T) \mathcal{M}. \quad (33)$$

The DIM/QM polarization gradients are rewritten by expanding the poly-tensor notation as

$$\begin{aligned}\nabla_{\delta} U^{\text{POL}}[\rho] &= -\sum_m \mu_{m,\alpha}^{\text{ind}} (\nabla_{\delta} E_{m,\alpha}^{\text{SCF}}) + \sum_m q_m^{\text{ind}} (\nabla_{\delta} V_m^{\text{SCF}}) \\ &= -\sum_m \mu_{m,\alpha}^{\text{ind}} \nabla_{\delta} E_{m,\alpha}^{\text{QM,el}} - \sum_m \mu_{m,\alpha}^{\text{ind}} \nabla_{\delta} E_{m,\alpha}^{\text{QM,nuc}} \\ &\quad + \sum_m q_m^{\text{ind}} \nabla_{\delta} V_m^{\text{QM,el}} + \sum_m q_m^{\text{ind}} \nabla_{\delta} V_m^{\text{QM,nuc}}.\end{aligned}\quad (34)$$

After taking the various derivatives of the nuclear and electronic fields and potentials only the derivatives of the density, $\rho(\mathbf{r}_j)$, and nuclear interaction tensors, $T_{jm}^{(0)}$ and $T_{jm,\alpha}^{(1)}$, are necessary because the electronic interaction tensors, $T_{jm}^{(0)}$ and $T_{jm,\alpha}^{(1)}$, are independent of the QM nuclei coordinates. Thus, the final form of the DIM/QM polarization gradients is

$$\begin{aligned}\nabla_{\delta} U^{\text{POL}}[\rho] &= +\sum_m \mu_{m,\alpha}^{\text{ind}} \left(\int (\nabla_{\delta} \rho(r_j)) T_{jm,\alpha}^{(1)} dr_j \right) \\ &\quad + \sum_m \mu_{m,\alpha}^{\text{ind}} (Z_K T_{Km,\alpha\delta}^{(2)}) \\ &\quad + \sum_m q_m^{\text{ind}} \left(\int (\nabla_{\delta} \rho(r_j)) T_{jm}^{(0)} dr_j \right) \\ &\quad + \sum_m q_m^{\text{ind}} (Z_K T_{Km,\delta}^{(1)}),\end{aligned}\quad (35)$$

where we use the equalities $T_{Km,\delta}^{(1)} = \nabla_{\delta} T_{jm}^{(0)}$ and $T_{Km,\alpha\delta}^{(2)} = \nabla_{\delta} T_{jm,\alpha}^{(1)}$.

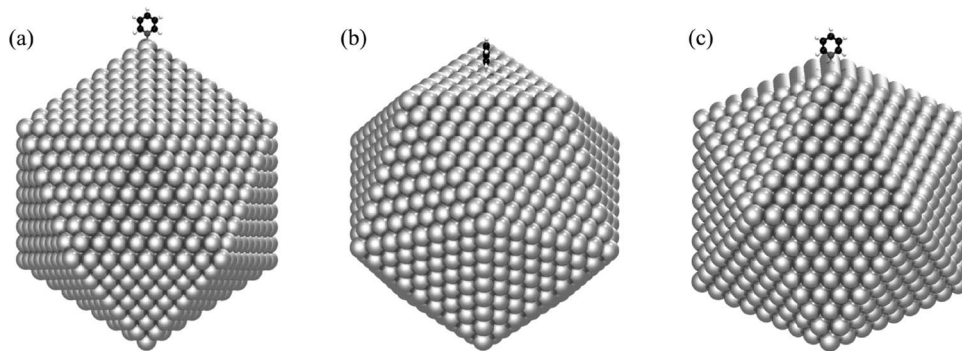


FIG. 1. The different pyridine adsorption sites of an icosahedral Ag_{2057} nanoparticle: (a) vertex, (b) face, and (c) edge adsorption site. Note the general orientation of the pyridine with respect to the nanoparticle depicted here is maintained for all icosahedral nanoparticle studied in this work.

The gradients arising from the purely classical forces of the LJ potential are straightforwardly given as

$$\nabla_{\delta} U^{\text{VDW}} = \sum_{Jm} \frac{-12\varepsilon_{Jm} r_{Jm,\delta}}{|\mathbf{r}_{Jm}|^2} \left[\left(\frac{r_{e,Jm}}{|\mathbf{r}_{Jm}|} \right)^{12} - \left(\frac{r_{e,Jm}}{|\mathbf{r}_{Jm}|} \right)^6 \right], \quad (36)$$

where again ε and r_e are the LJ parameters as discussed in Sec. II A.

C. Short-range screening of the interaction tensors

The general form of the interaction tensors are given by Eq. (10). In order to avoid over-polarization when solving the linear DIM equations (Eq. (11)), we introduce a damping at small distances. This ensures that there is no “polarizability catastrophe,”⁷⁰ (i.e., the equations diverge as the distance tends to zero). We adopt the renormalized interaction tensors proposed by Mayer,⁷¹ which is an extension of an earlier model by Jensen *et al.*⁷² The renormalized form of the $T_{mn}^{(0)}$, $T_{mn,\alpha}^{(1)}$, and $T_{mn,\alpha\beta}^{(2)}$ tensors are given in Ref. 47, where the dipoles and charges are considered as having a Gaussian distribution rather than being points.

In our previous work, we had replaced the point charges and dipoles in Eqs. (4), (5) and (35) with a Gaussian distribution having a unit width to account for screening of the DIM–QM atom interactions.^{72–74} We found this leads to over-polarization of the quantum system when the pyridine is chemisorbed, and therefore introduce the following damping function:⁴²

$$f_s = (1 - e^{-a|\mathbf{r}_{Jm}|})^n, \quad (37)$$

which results in a more effective screening. Here $n = 2$ for the screening of the potential (V^{SCF}) and $n = 3$ for the screening of the field (E^{SCF}).

III. COMPUTATIONAL METHODS

The DIM/QM analytical energies and gradients are implemented in a local development version of the Amsterdam Density Functional (ADF) software package. The structure and binding energies of a pyridine molecule at various adsorption sites of Ag_{20} tetrahedron are calculated using the BP86 functional,^{75,76} Slater-type orbitals, and a polarized triple- ζ (TZP) basis set from the ADF basis set library. The core orbitals (Ag[1s2s3s2p3p3d], N[1s], and C[1s]) are frozen,

and the zeroth-order regular approximation^{77,78} is employed to account for relativistic effects. The calculations are done both with and without the inclusions of Grimme’s D3 dispersion correction.⁷⁹ These calculations are used as a database to parametrize the coordination dependent LJ parameters for Ag and chemisorbed N.

All DIM/QM calculations are performed on a pyridine molecule adsorbed to the various sites (i.e., vertex, face, and edge) of a silver icosahedron nanoparticle (see Figure 1), with the pyridine being modeled with QM and the nanoparticle being modeled with DIM. We present nanoparticles of sizes from 147 to 10179 atoms, or 1–8 nm diameter, where the Ag–Ag bond length is set to the experimental distance of 2.889 Å. In all the calculations, the geometry of the QM atoms is fully optimized, followed by a vibrational frequencies analysis and then the computation of the Raman cross sections, all using the DIM/QM method. The vibrational frequencies are computed by a three point numerical differentiation of the analytical gradients; no imaginary frequencies are found. All DIM/QM computations of the structure, vibrational frequencies, polarizability, and Raman spectra employ the BP86/TZP level of theory. The BP86 functional is chosen for this study because of its good agreement with experimental vibrational frequencies as discussed in Ref. 34.

The Raman differential cross sections ($d\sigma/d\Omega$) are computed with a setup where the scattering angle is 90° and incident light is perpendicular plane-polarized as^{80,81}

$$I^k = \frac{d\sigma}{d\Omega} = \frac{\pi^2}{\epsilon_0^2} (\tilde{\nu}_{\text{in}} - \tilde{\nu}_k)^4 \frac{h}{8\pi^2 c \tilde{\nu}_k} [45\bar{\alpha}_k'^2 + 7\gamma_k'^2] \times \frac{1}{45(1 - \exp(-hc\tilde{\nu}_k/k_B T))}, \quad (38)$$

where $\tilde{\nu}_{\text{in}}$ and $\tilde{\nu}_k$ are the frequencies of the incident light and the k th vibrational mode, respectively. $\bar{\alpha}_k'$ and γ_k' are the isotropic and anisotropic polarizability derivatives with respect to the vibrational mode k and are computed by three point numerical differentiation of the polarizability (real and imaginary parts) with respect to the normal mode’s coordinates. The Raman scattering factor is defined as $[45\bar{\alpha}_k'^2 + 4\gamma_k'^2]$. This method relies on a short-time approximation to the Raman scattering and is based on a Placzek-like approximation which neglects the difference in the frequency of the incident and scattered light.⁸⁰

TABLE I. Bond lengths and binding energies for the different pyridine-Ag₂₀ adsorption sites. All computations used a TZP basis set, and the DIM/QM calculations employed the BP86 functional.

Site	R_{N-Ag} (Å)			Sites	Energies (kcal/mol)		
	BP86	BP86-D3	DIM/QM		BP86	BP86-D3	DIM/QM
Vertex	2.30	2.29	2.28	Vertex	-13.1	-16.7	-16.6
Face	2.46	2.40	2.39	Face	-5.31	-16.7	-15.8
Edge	2.41	...	2.34	Edge	-6.84	...	-16.0

The DIM/QM calculations of the frequency-dependent polarizability use a lifetime (Γ) of 0.1 eV as previously suggested in the literature.^{34,80,82,83} The polarization term of DIM/QM is screened as discussed in Sec. II C. For the damping function (Eq. (37)), we find a screening factor of $a = 1.0$ bohr⁻¹ appropriate. With this value we could correctly describe both the chemisorbed pyridine and physisorbed through the π -system (data not shown). The frequency-dependent polarizability ($\alpha_{m,\alpha\beta}(\omega)$) and capacitance ($c_m(\omega)$) DIM parameters for the Ag atoms are taken from Ref. 50. For the coordination dependent LJ parameters, the cutoff values for the effective coordination number of Ag are set to 3.0 and 5.0 Å for $|r_{\min}|$ and $|r_{\max}|$, respectively, as previously reported.⁵⁶ The chemisorption cutoff of N is set to $|r_{Jm}| = 2.60$ Å. All other LJ parameters are taken from the AMBER force field.⁵⁵

IV. RESULTS

A. Parametrization of the force field

The coordination-dependent LJ parameters for Ag and N needed to describe the adsorption of pyridine on the silver nanoparticles are obtained by fitting the parameters to full QM data. For our reference data, we consider pyridine adsorbed via the lone pair onto the vertex, face, and edge of a tetrahedral Ag₂₀ cluster. The Ag-N bond lengths and binding energies calculated using BP86/TZP and BP86-D3/TZP for different adsorption sites are collected in Table I. From these results, we observe that including dispersion correction has a significant effect on the results. This is in agreement with previous work, which shows that dispersion is important for molecular adsorption on surfaces.⁸⁴⁻⁸⁸ For both the vertex and the face adsorption site, a shortening of the bond length and increase in the magnitude of the binding energy is observed when including the D3 correction. This is especially true for the face site where the binding energy's magnitude is increased by around 10 kcal/mol. The edge site does not have a stable minimum for adsorption via the lone pair for the D3 correction, but rather has a minimum by adsorption to surface via the π system. After inclusion of the dispersion correction, the binding energy for the face and vertex sites are nearly identical; however, the origin of the binding energies are quite different. For the vertex site, the binding energy is dominated by chemisorption interactions between the N and Ag atoms, whereas for the face site the binding energy is dominated by dispersion interactions.

Due to the importance of the dispersion corrections, we choose to parametrize the classical force field against

the BP86-D3 results. The optimized parameters are listed in Table II together with the standard parameters adapted from the AMBER force field. In Table I, the DIM/QM Ag-N bond lengths and binding energies are presented for pyridine adsorbed onto the vertex, face, and edge of a tetrahedral Ag₂₀ cluster. We find that the DIM/QM results are reasonable for the different adsorption sites.

B. Adsorption of pyridine onto icosahedral nanoparticles

The geometry of pyridine has been optimized while interacting with different icosahedral Ag nanoparticles of sizes ranging from 147 to 10179 atoms. We examine three different adsorption sites (illustrated in Figure 1) for pyridine on a Ag₂₀₅₇ nanoparticle. Overall, only small changes in the ground state geometry of the pyridine molecules are observed once adsorbed onto the metal surface. The biggest change is the CNC bond angle which decreases by around 3° as compared to the gas phase structure. In Figure 2, we plot the Ag-N bond length and the binding energy as a function of the nanoparticle's size for the three different adsorption sites. From the figure, we observe that the Ag-N bond lengths converge to 2.34, 2.38, and 2.43 Å for the vertex, edge, and face site, respectively. This is consistent with the results obtained for the small Ag₂₀ cluster although the bond length is slightly longer in all three cases. This is likely a result of the different effective coordination environments of the icosahedral Ag nanoparticle versus the small tetrahedral Ag₂₀ cluster. We also see that there is almost no dependence of the Ag-N bond length on the nanoparticle's size.

The binding energy saturates around 15.7, 16.8, and 19.0 kcal/mol for the vertex, edge, and face site, respectively. The binding energies are consistent with the results for the Ag₂₀ cluster, although the face site is found to be strongest for this nanoparticle. This points to the fact that dispersion effects are important for these large nanoparticles. This is particularly evident for the face adsorption site since it has the lowest

TABLE II. LJ parameters used in the force field. The Van der Waals equilibrium bond lengths, r_e , are in Å while the well depths, ϵ , are in kcal/mol. r_e and ϵ are taken from the AMBER force field.⁵⁶

Atom type	r_e	ϵ	r_0	r_1	ϵ_0	ϵ_1
H	1.459	0.0150				
C	1.908	0.0860				
N	1.824	0.1700	0.4233	0.4763	172.56	32.944
Ag			1.7198	1.9315	1.8825	0.5020

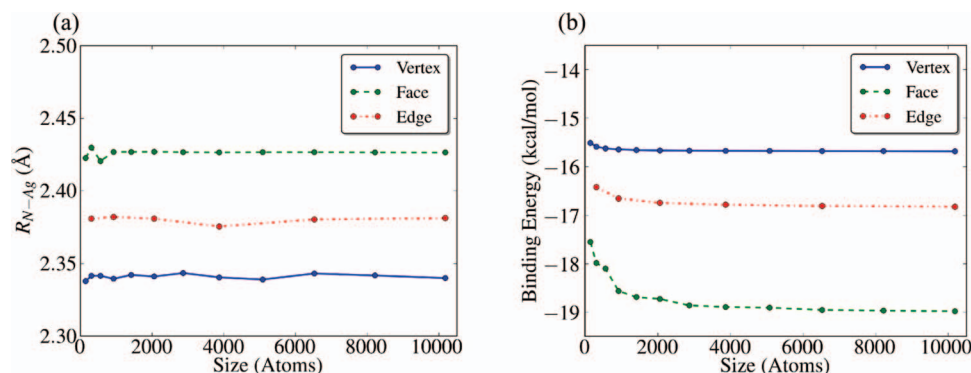


FIG. 2. (a) The Ag-N bond lengths and (b) the binding energies of pyridine on to the icosahedral nanoparticle as function of the nanoparticle's size for the vertex, face, and edge adsorption sites.

binding energy but the longest bond length. Similar to the bond lengths, we find only modest dependence of the binding energy on the size of the nanoparticle. In fact, only the face site shows a dependence between binding energy and size; lowering about 2 kcal/mol from Ag_{147} to Ag_{2057} . The binding energy in Figure 2(b) is dominated by the U^{VDW} while on average U^{POL} is about 5~15% of the total binding energy.

C. Raman spectra of pyridine adsorbed on icosahedral silver nanoparticles

For the Raman scattering of pyridine, we simulate the Raman spectra of pyridine adsorbed onto silver nanoparticles

sized between 147 and 10179 atoms at each adsorption site. Figure 3 shows the simulated Raman spectra of free pyridine compared to pyridine adsorbed on the three different adsorption sites of an icosahedral Ag_{6525} nanoparticle with the incident light at 413.3 nm. For the free pyridine there are six Raman active modes (at 598, 649, 979, 1021, 1204, and 1573 cm^{-1}) with significant intensity between 300 and 1600 cm^{-1} . Except for the mode at 649 cm^{-1} , these are also the intense modes when adsorbed on the metal nanoparticle. The relative intensities of the Raman spectra of pyridine for the three different adsorption sites are fairly similar which is expected because of their similar geometries. However, there is significant variation in the absolute intensities of the

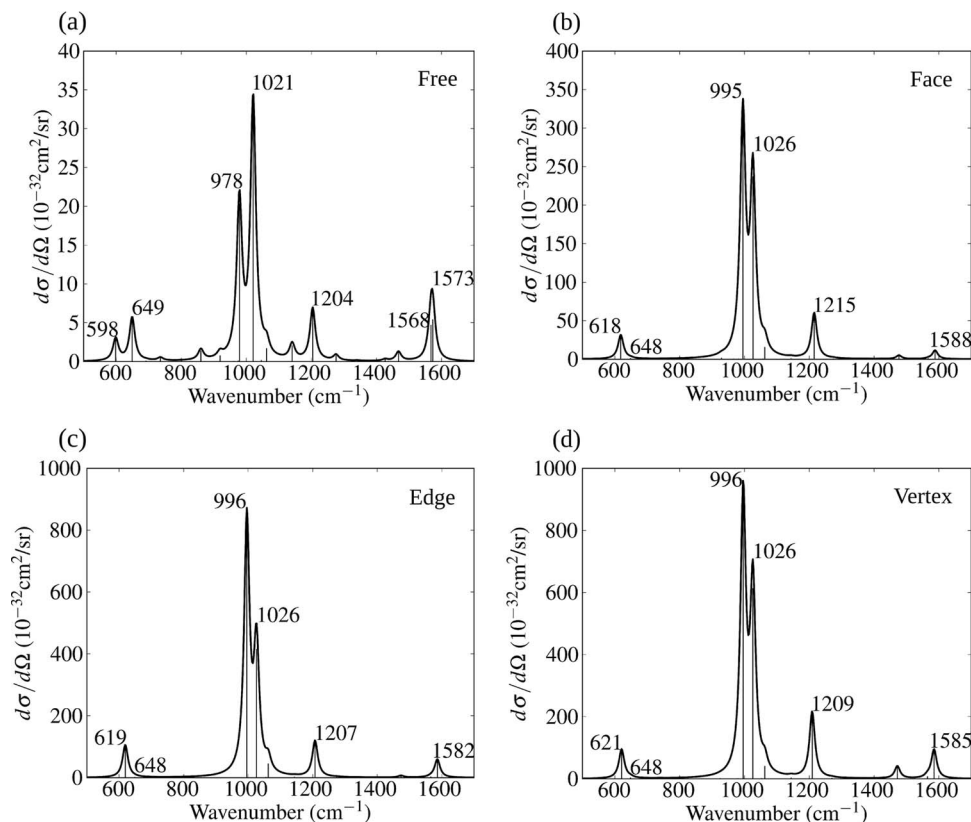


FIG. 3. Simulated Raman spectra of (a) free pyridine, (b) pyridine- Ag_{6525} face site, (c) pyridine- Ag_{6525} edge site, and (d) pyridine- Ag_{6525} vertex site. All spectra are calculated at 413.3 nm ($\omega = 3.000$ eV). $d\sigma/d\Omega$ is the differential cross section. Spectral broadening has been applied assuming a Lorentzian having a full width at half max of 20 cm^{-1} .

TABLE III. Shifts in the harmonic frequencies ($\Delta\nu = \nu^{\text{Adsorbed}} - \nu^{\text{Free}}$) in cm^{-1} for pyridine on three different sites of an icosahedral Ag_{6525} nanoparticle. For comparison the full BP86/TZP data of pyridine adsorbed on a Ag_{20} cluster taken from Ref. 91 as well as experimental data for pyridine on a roughened Ag surface taken from Ref. 22.

Method	Site	Size	598	649	979	1021	1204	1573
QM	Vertex	Ag_{20}	22	-2	18	3	-2	15
QM	Face	Ag_{20}	14	-2	13	0	-5	8
DIM/QM	Vertex	Ag_{6525}	23	-1	17	5	5	12
DIM/QM	Face	Ag_{6525}	20	-1	17	5	11	15
DIM/QM	Edge	Ag_{6525}	21	-1	17	5	3	13
Exp.	Roughened Ag		22	-1	17	6	-1	-3

Raman scattering, with the vertex site being the strongest, followed by the edge site, and then the face site. The enhancements are rather modest and on the order of about a factor of 100. There is good agreement between the DIM/QM simulated spectra and both previous experimental work⁸⁹ and theoretical simulation using either fully QM (Ref. 34) or other hybrid approaches.^{45,90} In the following, we will analyze the enhanced Raman spectra in more detail.

First, the shifts in the harmonic frequencies of the pyridine adsorbed on an icosahedral Ag_{6525} nanoparticle relative to the free molecule (i.e., $\Delta\nu = \nu^{\text{Adsorbed}} - \nu^{\text{Free}}$) are collected in Table III. In the table, we have also listed previously reported QM results⁹¹ for pyridine on the tetrahedral Ag_{20} cluster and experimental results.²² We observe that the shifts in vibrational frequencies obtained using DIM/QM are rather similar between the three different adsorption sites. The three modes that change the most are at 598, 979, and 1573 cm^{-1} . This is not surprising, since in these modes the nitrogen atom is being displaced along the Ag–N bond and therefore experiences the largest perturbations when adsorbed on the metal nanoparticle. Overall, the DIM/QM results are in good agreement with the both the full QM results and experiments for the magnitude and direction of the shifts. The one exception is the mode at 1204 cm^{-1} where the DIM/QM results show an increase in frequency by $3\text{--}11 \text{ cm}^{-1}$ whereas the QM and experiments show a small decrease in the vibrational frequency.

The icosahedral nanoparticles studied in this work are characterized by a strong, broad (i.e., the full width at half

maximum is $\sim 1 \text{ eV}$) absorption band around 3.7 eV due to the plasmon excitation. The broad plasmon excitation is a result of increased surface scattering due to the small size of the nanoparticle.⁴⁸ We calculate the Raman scattering factor of pyridine as a function of the incident light's frequency using DIM/QM to examine the importance of the plasmon on the Raman scattering. In Figure 4(a), we plot the cross section for the $\nu = 978 \text{ cm}^{-1}$ mode of pyridine adsorbed on an icosahedral Ag_{6525} nanoparticle for the three different adsorption sites between 2.75 and 4.5 eV . We limit the frequency range to this window because this is the range in which the Ag CPIM parameters were parametrized.⁴⁸ From the figure, we find a strong dependence on the frequency of the incident light and that the behavior is different for the three adsorption sites. For the edge and face sites, the Raman cross section shows a maximum at 3.5 and 3.7 eV , respectively; while for the vertex site the maximum is around 3.0 eV . Thus, the edge and face sites show a wavelength dependence following the plasmon excitation, whereas the vertex site does not.

In Figure 4(b), we plot the polarizability squared (i.e., $\alpha(\omega)^2 = \alpha(\omega)\alpha(\omega)^*$, where $\alpha(\omega)^*$ is the complex conjugate of the polarizability) for pyridine on the Ag_{6525} nanoparticle calculated using DIM/QM. This is done to understand in more detail the trends seen in Figure 4(a). The polarizability calculated using DIM/QM contains the polarizability of the molecule under the influence of the image and local field and the polarizability induced into the metal nanoparticle from the interactions with the molecule.⁵⁰ The polarizability of the isolated Ag_{6525} nanoparticle is excluded from the spectrum since it is independent of molecular vibrations and thus does not contribute to the Raman scattering factor. We observe a good agreement between $\alpha(\omega)^2$ and the Raman scattering factor for all three adsorption sites. The Raman scattering factor are proportional to the polarizability derivative with respect to the normal mode squared, $(\partial\alpha(\omega)/\partial Q)^2$. Since the molecular vibrations do not appreciably change in the presence of the nanoparticle compared to free pyridine, it is reasonable that this quantity would roughly scale with the polarizability squared, which is what is seen when comparing Figures 4(a) and 4(b). It is important to stress that both the real and imaginary components contribute to $\alpha(\omega)^2$ (and thus also $(\partial\alpha(\omega)/\partial Q)^2$), which is typical of a resonance Raman effect.

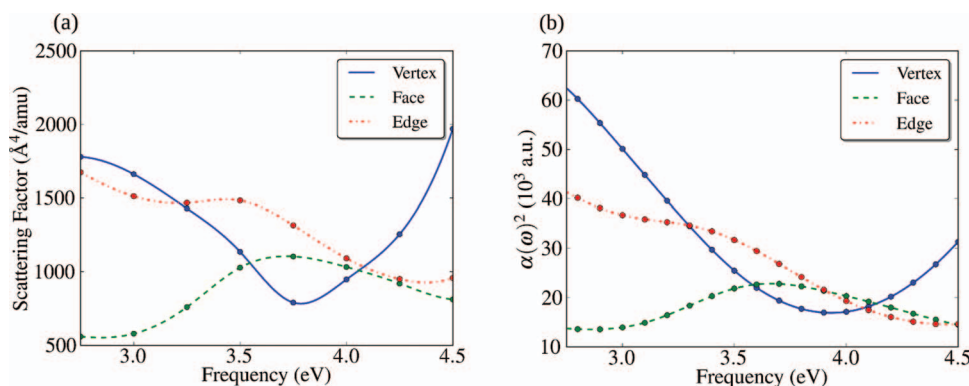


FIG. 4. (a) The Raman differential cross section for the pyridine mode at $\nu = 978 \text{ cm}^{-1}$ and (b) the DIM/QM polarizability squared ($\alpha(\omega)^2 = \alpha(\omega)\alpha(\omega)^*$) of the pyridine adsorbed on an icosahedral Ag_{6525} nanoparticle.

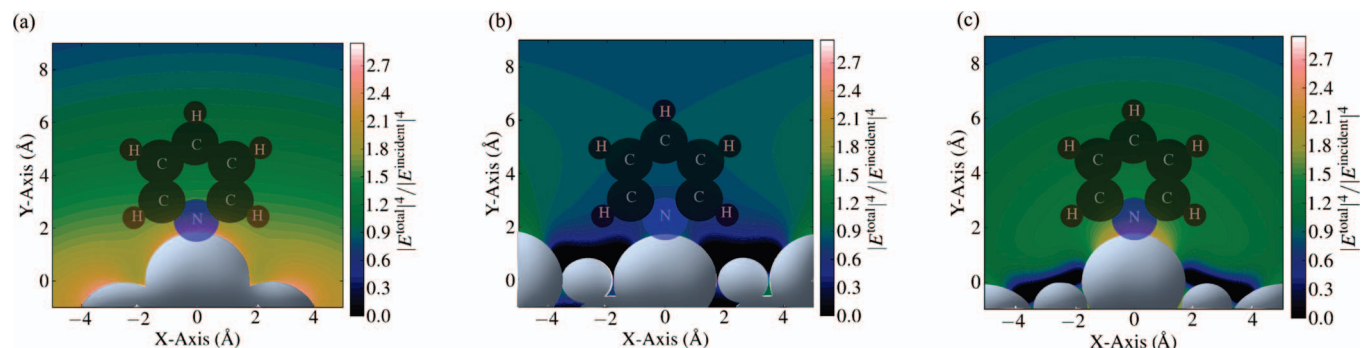


FIG. 5. The local field enhancements for the nanoparticle at the (a) vertex, (b) face, and (c) edge adsorption site. The field enhancements are plotted on a log scale for an incident light of $\omega = 3.0$ eV. The Ag atom bonded to the nitrogen is at the origin while pyridine is on the xy-plane.

The dominant mechanism for the enhanced polarizability in DIM/QM is the interaction between the local field and the molecule. Therefore, we calculate the local field around the pyridine molecule arising from the induced dipoles and charges obtained in the DIM/QM simulations. In Figure 5, we depict the local field enhancement factors, $|E^{\text{total}}|^4/|E^{\text{incident}}|^4$, with $\omega = 3.0$ eV for the three adsorption sites of a Ag_{6525} nanoparticle. For the vertex site, we clearly see a strong local field enhancement which increases in magnitude as the size of the nanoparticle increases. This is consistent with the idea that sharp points, like the vertex site, create “hot spots” where the local electric field is large. In contrast for the face adsorption site, it is observed that the local field enhancement tends to decrease as the nanoparticle’s size increases; where the local electric fields about the face are largest only for the smallest particle studied in this work. One rationale is that for smaller nanoparticles the face site is close to three vertices all with high local electric fields whereas for the bigger particles the vertices are far from the face site. The local field enhancement about the edge site remains at a relatively constant magnitude over the nanoparticle sizes ranging from 309 to 3871 atoms, after which the fields begin to increase in a fashion similar to the vertex site. A possible reason for this observed behavior is the edge site can adopt both face-like and vertex-like attributes for the small and large particles, respectively.

The enhancement factors based on the local fields are between a factor of 10 and 100, in good agreement with the observed enhancements of the Raman spectra presented in

Figure 3. However, we do see that the enhancement factors vary significantly over the distance of the molecule, illustrating the approximate nature of using $|E^{\text{total}}|^4/|E^{\text{incident}}|^4$ as a measure of the observed enhancements. The largest field enhancements are found around $\omega = 3.0$ eV, which do not correlate with the maximum of the plasmon excitation. This is typical of broad plasmon peaks and have, for example, been found experimentally and theoretically for SERS of Pt nanoparticles to be a result of Fano interference between the free plasmon excitation and continuum interband transitions.⁹²

One would expect that the enhancement of the Raman scattering increases as the size of the nanoparticle increases due to the stronger local fields. However, as discussed above, this is not necessarily true since the enhancement depends strongly on both the adsorption site and the frequency of the incident light. In Figure 6, we plot the Raman spectra of pyridine as a function of the nanoparticle’s size for the three different adsorption sites. In the simulations, we take the incident light to be $\omega = 3.0$ eV, which is where the largest field enhancements are found. From the figure, we find a significantly different size-dependence of the Raman scattering for the three adsorption sites. For the vertex site, we observe a steady increase in the Raman cross sections as the size of the cluster increases. In contrast, the face site shows the largest enhancements for the smallest particles, and the enhancements for the edges site are fairly constant for the larger sizes. The trends in Raman enhancement for the different adsorption sites as a function of size mirrors the behavior observed

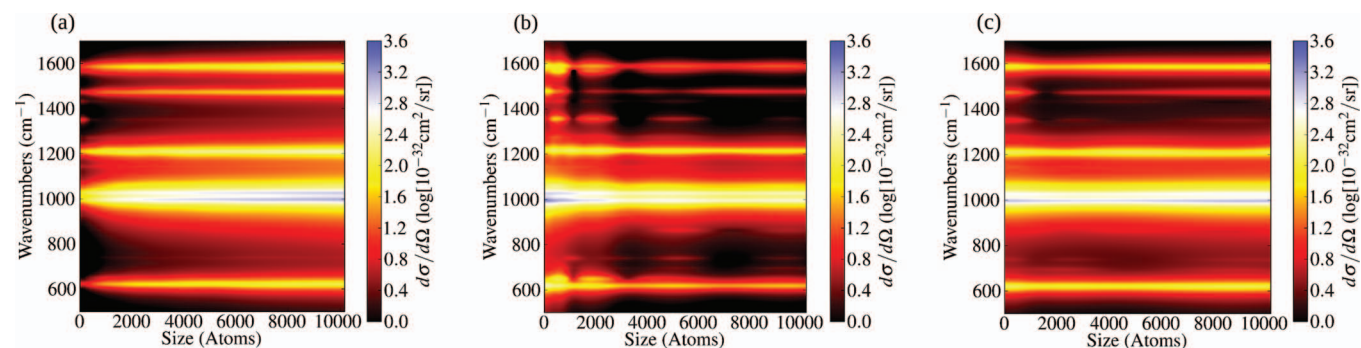


FIG. 6. The Raman differential cross section of pyridine at three adsorption sites, (a) vertex, (b) face, and (c) edge, plotted as function of the icosahedral nanoparticle’s size. Note that the cross section is plotted on a log scale and all spectra were computed with an incident frequency of $\omega = 3.0$ eV.

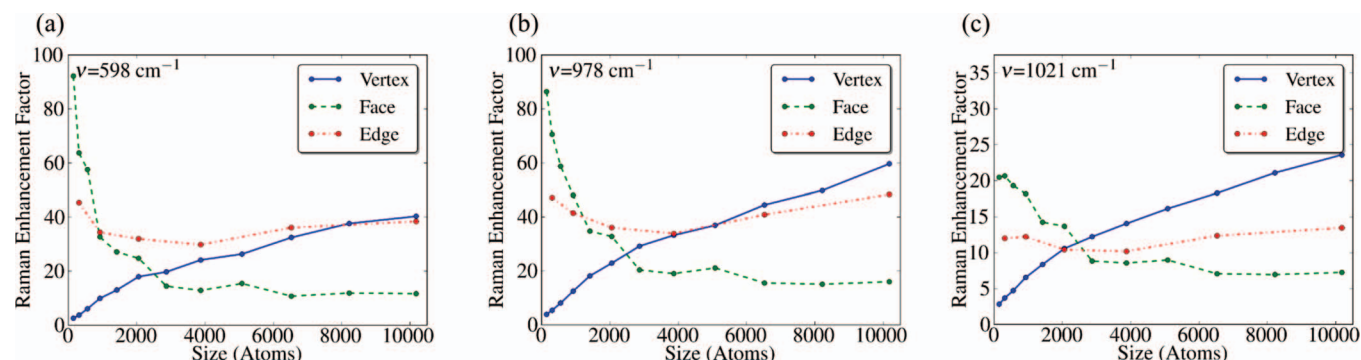


FIG. 7. The Raman enhancement factors (EF_k) of pyridine at the three adsorption sites (vertex, face, and edge) for the modes at $\nu =$ (a) 598, (b) 978, and (c) 1021 cm^{-1} obtained with an incident frequency of $\omega = 3.0$ eV.

for the local field enhancements as discussed above, which supports the fact that the enhancements here are due to the local fields. All results also indicate a strong dependence on the nanoparticles' local environments for the Raman spectra and highlight the importance of an atomistic description of the system.

To better quantify the size-dependence of the Raman scattering observed for pyridine on the metal nanoparticles, we plot in Figure 7 the calculated Raman enhancement factors for the three strong modes at $\nu = 598$, 978, and 1021 cm^{-1} . The enhancement factor for each mode k is calculated as $EF_k = I_{\text{adsorbed}}^k(\omega)/I_{\text{free}}^k(\omega)$, where $I_{\text{adsorbed}}^k(\omega)$ and $I_{\text{free}}^k(\omega)$ are the frequency dependent differential cross sections of pyridine adsorbed to the metal nanoparticle and in free space, respectively. For all three modes we see the enhancement for the vertex increase with size, the face decrease and plateau with size, and the edge remain fairly constant. These trends are also observed for the Raman spectra using an incident wavelength of $\omega = 3.75$ eV for all three sites, although less dramatic. Full QM simulations also find that for small metal clusters, the face site shows stronger Raman enhancements than the vertex site.³⁴ This is likely because the small face site experiences the local field from several nearby vertices. The calculated enhancement factors range between a factor of 10–100 which is consistent with the electric field enhancements plotted in Figure 5. The modest enhancements are due to the small size of the nanoparticles which lead to broad plasmon resonance and small field enhancements.

V. CONCLUSION

In this work we have derived and implemented analytical gradients for DIM/QM such that geometry optimization, vibrational frequencies, and Raman spectra can be simulated for molecules interacting with metal nanoparticles. As a test of the implementation, we simulated the SERS spectra for pyridine adsorbed on different sites of icosahedral nanoparticles with diameters between 1 and 8 nm. To describe the adsorption of the pyridine molecule onto the metal nanoparticle, we implemented a coordination-dependent force field such that the different adsorption sites could be correctly described. We found that the DIM/QM method predicted geometries and frequencies in good agreement with full

QM simulations and experiments. For the simulated SERS spectra of pyridine, we found a significant dependence of the adsorption site and the size of the metal nanoparticle. This illustrated the importance of accounting for the local environment around the molecule. Modest enhancement factors were obtained due to the broad plasmon peak found for the small nanoparticles used in this work. We found that the Raman enhancement factors followed approximately the local field enhancements.

ACKNOWLEDGMENTS

L.J. acknowledges the CAREER program of the National Science Foundation (NSF) (Grant No. CHE-0955689) for financial support, start-up funds from the Pennsylvania State University, and support received from Research Computing and Cyberinfrastructure, a unit of Information Technology Services at Penn State. S.M.M. acknowledges the Academic Computing Fellowship from the Pennsylvania State University Graduate School.

- ¹H. A. Atwater and A. Polman, *Nature Mater.* **9**, 205 (2010).
- ²V. E. Ferry, J. N. Munday, and H. A. Atwater, *Adv. Mater.* **22**, 4794 (2010).
- ³K. Kneipp, H. Kneipp, I. Itzkan, R. R. Dasari, and M. S. Feld, *Chem. Rev.* **99**, 2957 (1999).
- ⁴C. A. Mirkin, R. L. Letsinger, R. C. Mucic, and J. J. Storhoff, *Nature (London)* **382**, 607 (1996).
- ⁵A. J. Haes, W. P. Hall, L. Chang, W. L. Klein, and R. P. Van Duyne, *Nano Lett.* **4**, 1029 (2004).
- ⁶C. R. Yonzon, C. L. Haynes, X. Zhang, J. T. Walsh, and R. P. Van Duyne, *Anal. Chem.* **76**, 78 (2004).
- ⁷P. Alivisatos, *Nat. Biotechnol.* **22**, 47 (2004).
- ⁸A. J. Haes, C. L. Haynes, A. D. McFarland, G. C. Schatz, R. P. Van Duyne, and S. Zou, *MRS Bull.* **30**, 368 (2005).
- ⁹N. L. Rosi and C. A. Mirkin, *Chem. Rev.* **105**, 1547 (2005).
- ¹⁰W. P. Halperin, *Rev. Mod. Phys.* **58**, 533 (1986).
- ¹¹S. Link and M. A. El-Sayed, *Ann. Rev. Phys. Chem.* **54**, 331 (2003).
- ¹²D. A. Stuart, J. M. Yuen, N. Shah, O. Lyandres, C. R. Yonzon, M. R. Glucksberg, J. T. Walsh, and R. P. Van Duyne, *Acta Crystallogr.* **78**, 7211 (2006).
- ¹³X. Huang, I. H. El-Sayed, W. Qian, and M. A. El-Sayed, *J. Am. Chem. Soc.* **128**, 2115 (2006).
- ¹⁴K. L. Kelly, E. Coronado, L. L. Zhao, and G. C. Schatz, *J. Phys. Chem. B* **107**, 668 (2003).
- ¹⁵M. Moskovits, *Rev. Mod. Phys.* **57**, 783 (1985).
- ¹⁶A. Campion and P. Kambhampati, *Chem. Soc. Rev.* **27**, 241 (1998).
- ¹⁷A. M. Michaels, M. Nirmal, and L. E. Brus, *J. Am. Chem. Soc.* **121**, 9932 (1999).
- ¹⁸H. Xu, E. J. Bjerneld, M. Käll, and L. Börjesson, *Phys. Rev. Lett.* **83**, 4357 (1999).

- ¹⁹J. A. Dieringer, R. B. Lettan, K. A. Scheidt, and R. P. Van Duyne, *J. Am. Chem. Soc.* **129**, 16249 (2007).
- ²⁰K. Kneipp, Y. Wang, H. Kneipp, L. T. Perelman, I. Itzkan, R. R. Dasari, and M. S. Feld, *Phys. Rev. Lett.* **78**, 1667 (1997).
- ²¹S. M. Nie and S. R. Emory, *Science* **275**, 1102 (1997).
- ²²D. L. Jeanmaire and R. P. Van Duyne, *J. Electroanal. Chem.* **84**, 1 (1977).
- ²³M. G. Albrecht and J. A. Creighton, *J. Am. Chem. Soc.* **99**, 5215 (1977).
- ²⁴L. Jensen, C. M. Aikens, and G. C. Schatz, *Chem. Soc. Rev.* **37**, 1061 (2008).
- ²⁵S. M. Morton, D. W. Silverstein, and L. Jensen, *Chem. Rev.* **111**, 3962 (2011).
- ²⁶J. Gersten and A. Nitzan, *J. Chem. Phys.* **73**, 3023 (1980).
- ²⁷E. C. Le Ru and P. G. Etchegoin, *Chem. Phys. Lett.* **423**, 63 (2006).
- ²⁸J. Zhao, A. O. Pinchuk, J. M. McMahon, S. Li, L. K. Ausman, A. L. Atkinson, and G. C. Schatz, *Acc. Chem. Res.* **41**, 1710 (2008).
- ²⁹F. J. García de Abajo, *J. Phys. Chem. C* **112**, 17983 (2008).
- ³⁰J. M. McMahon, S. K. Gray, and G. C. Schatz, *Phys. Rev. Lett.* **103**, 097403 (2009).
- ³¹J. Zuloaga, E. Prodan, and P. Nordlander, *Nano Lett.* **9**, 887 (2009).
- ³²J. Zuloaga, E. Prodan, and P. Nordlander, *ACS Nano* **4**, 5269 (2010).
- ³³S. M. Morton and L. Jensen, *J. Am. Chem. Soc.* **131**, 4090 (2009).
- ³⁴L. Zhao, L. Jensen, and G. C. Schatz, *J. Am. Chem. Soc.* **128**, 2911 (2006).
- ³⁵S. Corni and J. Tomasi, *J. Chem. Phys.* **114**, 3739 (2001).
- ³⁶S. Corni and J. Tomasi, *J. Chem. Phys.* **117**, 7266 (2002).
- ³⁷S. Corni and J. Tomasi, *J. Chem. Phys.* **116**, 1156 (2002).
- ³⁸S. Vukovic, S. Corni, and B. Mennucci, *J. Phys. Chem. C* **113**, 121 (2009).
- ³⁹S. Jørgensen, M. A. Ratner, and K. V. Mikkelsen, *J. Chem. Phys.* **115**, 3792 (2001).
- ⁴⁰D. Neuhauser and K. Lopata, *J. Chem. Phys.* **127**, 154715 (2007).
- ⁴¹K. Lopata and D. Neuhauser, *J. Chem. Phys.* **130**, 104707 (2009).
- ⁴²V. Arcisauskaitė, J. Kongsted, T. Hansen, and K. V. Mikkelsen, *Chem. Phys. Lett.* **470**, 285 (2009).
- ⁴³D. J. Masiello and G. C. Schatz, *Phys. Rev. A* **78**, 042505 (2008).
- ⁴⁴D. J. Masiello and G. C. Schatz, *J. Chem. Phys.* **132**, 064102 (2010).
- ⁴⁵H. Chen, J. M. McMahon, M. A. Ratner, and G. C. Schatz, *J. Phys. Chem. C* **114**, 14384 (2010).
- ⁴⁶M. A. Watson, D. Rappoport, E. M. Y. Lee, R. Olivares-Amaya, and A. Aspuru-Guzik, *J. Chem. Phys.* **136**, 024101 (2012).
- ⁴⁷L. L. Jensen and L. Jensen, *J. Phys. Chem. C* **112**, 15697 (2008).
- ⁴⁸L. L. Jensen and L. Jensen, *J. Phys. Chem. C* **113**, 15182 (2009).
- ⁴⁹S. M. Morton and L. Jensen, *J. Chem. Phys.* **133**, 074103 (2010).
- ⁵⁰S. M. Morton and L. Jensen, *J. Chem. Phys.* **135**, 134103 (2011).
- ⁵¹J. Kongsted, A. Osted, K. V. Mikkelsen, and O. Christiansen, *J. Chem. Phys.* **118**, 1620 (2003).
- ⁵²J. Kongsted, A. Osted, K. V. Mikkelsen, and O. Christiansen, *J. Chem. Phys.* **119**, 10519 (2003).
- ⁵³J. Kongsted, A. Osted, K. V. Mikkelsen, and O. Christiansen, *J. Chem. Phys.* **120**, 3787 (2004).
- ⁵⁴C. J. Böttcher, *Theory of Electric Polarisation*, 1st ed. (Elsevier, London, 1952).
- ⁵⁵W. D. Cornell, P. Cieplak, C. I. Bayly, I. R. Gould, K. M. Merz, D. M. Ferguson, D. C. Spellmeyer, T. Fox, J. W. Caldwell, and P. A. Kollman, *J. Am. Chem. Soc.* **117**, 5179 (1995).
- ⁵⁶N. Legenski, C. Zhou, Q. Zhang, B. Han, J. Wu, L. Chen, H. Cheng, and R. C. Forrey, *J. Comput. Chem.* **32**, 1711 (2011).
- ⁵⁷J. E. Demuth, K. Christmann, and P. N. Sanda, *Chem. Phys. Lett.* **76**, 201 (1980).
- ⁵⁸M. Bader, J. Haase, K.-H. Frank, A. Puschmann, and A. Otto, *Phys. Rev. Lett.* **56**, 1921 (1986).
- ⁵⁹M. Moskovits, D. P. DiLella, and K. J. Maynard, *Langmuir* **4**, 67 (1988).
- ⁶⁰J.-G. Lee, J. Ahner, and J. T. Yates, Jr., *J. Chem. Phys.* **114**, 1414 (2001).
- ⁶¹J. R. Hahn and W. Ho, *J. Chem. Phys.* **124**, 204708 (2006).
- ⁶²J. A. Creighton, M. G. Albrecht, R. E. Hester, and J. A. D. Matthew, *Chem. Phys. Lett.* **55**, 55 (1978).
- ⁶³W. Krasser, U. Kettler, and P. S. Bechthold, *Chem. Phys. Lett.* **86**, 223 (1982).
- ⁶⁴J. Applequist, *J. Chem. Phys.* **83**, 809 (1985).
- ⁶⁵C. C. Pye and T. Ziegler, *Theor. Chem. Acc.* **101**, 396 (1999).
- ⁶⁶H. Li, H. M. Netzloff, and M. S. Gordon, *J. Chem. Phys.* **125**, 194103 (2006).
- ⁶⁷H. Li and M. S. Gordon, *J. Chem. Phys.* **126**, 124112 (2007).
- ⁶⁸Y. Wang and H. Li, *J. Chem. Phys.* **133**, 034108 (2010).
- ⁶⁹D. Si and H. Li, *J. Chem. Phys.* **133**, 144112 (2010).
- ⁷⁰B. T. Thole, *Chem. Phys.* **59**, 341 (1981).
- ⁷¹A. Mayer, *Phys. Rev. B* **75**, 045407 (2007).
- ⁷²L. Jensen, P. van Duijnen, and J. Snijders, *J. Chem. Phys.* **119**, 3800 (2003).
- ⁷³L. Jensen, P. Astrand, A. Osted, J. Kongsted, and K. Mikkelsen, *J. Chem. Phys.* **116**, 4001 (2002).
- ⁷⁴L. Jensen, P. T. van Duijnen, and J. G. Snijders, *J. Chem. Phys.* **118**, 514 (2003).
- ⁷⁵A. D. Becke, *Phys. Rev. A* **38**, 3098 (1988).
- ⁷⁶J. P. Perdew, *Phys. Rev. B* **33**, 8822 (1986).
- ⁷⁷E. van Lenthe, E. J. Baerends, and J. G. Snijders, *J. Chem. Phys.* **99**, 4597 (1993).
- ⁷⁸E. van Lenthe, E. J. Baerends, and J. G. Snijders, *J. Chem. Phys.* **101**, 9783 (1994).
- ⁷⁹S. Grimme, J. Antony, S. Ehrlich, and H. Krieg, *J. Chem. Phys.* **132**, 154104 (2010).
- ⁸⁰L. Jensen, L. L. Zhao, J. Autschbach, and G. C. Schatz, *J. Chem. Phys.* **123**, 174110 (2005).
- ⁸¹J. Neugebauer, M. Reiher, C. Kind, and B. A. Hess, *J. Comput. Chem.* **23**, 895 (2002).
- ⁸²L. Jensen, J. Autschbach, and G. C. Schatz, *J. Chem. Phys.* **122**, 224115 (2005).
- ⁸³L. L. Zhao, L. Jensen, and G. C. Schatz, *Nano Lett.* **6**, 1229 (2006).
- ⁸⁴A. Bilic, J. R. Reimers, and N. S. Hush, *J. Phys. Chem. B* **106**, 6740 (2002).
- ⁸⁵F. Ortmann, W. G. Schmidt, and F. Bechstedt, *Phys. Rev. Lett.* **95**, 186101 (2005).
- ⁸⁶S. D. Chakarova-Kack, E. Schroder, B. I. Lundqvist, and D. C. Langreth, *Phys. Rev. Lett.* **96**, 146107 (2006).
- ⁸⁷E. Rauls, S. Blankenburg, and W. G. Schmidt, *Surf. Sci.* **602**, 2170 (2008).
- ⁸⁸N. Atodiresei, V. Caciuc, P. Lazic, and S. Blugel, *Phys. Rev. Lett.* **102**, 136809 (2009).
- ⁸⁹J. T. Golab, J. R. Sprague, K. T. Carron, G. C. Schatz, and R. P. Van Duyne, *J. Chem. Phys.* **88**, 7942 (1988).
- ⁹⁰S. Corni and J. Tomasi, *Chem. Phys. Lett.* **342**, 135 (2001).
- ⁹¹L. Jensen, L. L. Zhao, and G. C. Schatz, *J. Phys. Chem. C* **111**, 4756 (2007).
- ⁹²Q. Hao, B. K. Juluri, Y. B. Zheng, B. Wang, I.-K. Chiang, L. Jensen, V. Crespi, P. C. Eklund, and T. J. Huang, *J. Phys. Chem. C* **114**, 18059 (2010).